UNIVERSITY OF AMSTERDAM

UvA-DARE (Digital Academic Repository)

Detection and Evolution of Linear Polarization of the Galactic Center Transient MAXI J1744-294

Michail, Joseph M.; von Fellenberg, Sebastiano D.; Balakrishnan, Mayura; Bower, Geoffrey C.; Ford, Nicole M.; Sumners, Zach; Fazio, Giovanni G.; Haggard, Daryl; Hora, Joseph L.; Keating, Garrett K.; Livingston, J.D.; Markoff, Sera; Ripperda, Bart; Sánchez-Maes, Sophia; Smith, Howard A.; Willner, S.P.; Zhao, Jun-Hui

DOI
10.3847/1538-4357/ae5dc8

Publication date
2026

Document Version
Final published version

Published in
Astrophysical Journal

License
CC BY

Link to publication

Citation for published version (APA):
Michail, J. M., von Fellenberg, S. D., Balakrishnan, M., Bower, G. C., Ford, N. M., Sumners, Z., Fazio, G. G., Haggard, D., Hora, J. L., Keating, G. K., Livingston, J. D., Markoff, S., Ripperda, B., Sánchez-Maes, S., Smith, H. A., Willner, S. P., & Zhao, J.-H. (2026). Detection and Evolution of Linear Polarization of the Galactic Center Transient MAXI J1744-294. *Astrophysical Journal*, *1003*(1), Article 38. https://doi.org/10.3847/1538-4357/ae5dc8

General rights
It is not permitted to download or to forward/distribute the text or part of it without the consent of the author(s) and/or copyright holder(s), other than for strictly personal, individual use, unless the work is under an open content license (like Creative Commons).

Disclaimer/Complaints regulations
If you believe that digital publication of certain material infringes any of your rights or (privacy) interests, please let the Library know, stating your reasons. In case of a legitimate complaint, the Library will make the material inaccessible and/or remove it from the website. Please Ask the Library: https://uba.uva.nl/en/contact, or a letter to: Library of the University of Amsterdam, Secretariat, P.O. Box 19185, 1000 GD Amsterdam, The Netherlands. You will be contacted as soon as possible.

UvA-DARE is a service provided by the library of the University of Amsterdam (https://dare.uva.nl)

Download date:09 Nov 2026

The Astrophysical Journal, 1003:38 (11pp), 2026 May 20 https://doi.org/10.3847/1538-4357/ae5dc8
© 2026. The Author(s). Published by the American Astronomical Society.
OPEN ACCESS

Detection and Evolution of Linear Polarization of the Galactic Center Transient MAXI J1744-294

Joseph M. Michail[1,15], Sebastiano D. von Fellenberg[2,3,16], Mayura Balakrishnan[4,5], Geoffrey C. Bower[6,7,8], Nicole M. Ford[4,5], Zach Sumners[4,5], Giovanni G. Fazio[1,17], Daryl Haggard[4,5], Joseph L. Hora[1], Garrett K. Keating[1], J. D. Livingston[3], Sera Markoff[9,10,11], Bart Ripperda[2,12,13], Sophia Sánchez-Maes[14], Howard A. Smith[1], S. P. Willner[1], and Jun-Hui Zhao[1]

[1] Center for Astrophysics |Harvard & Smithsonian, 60 Garden Street, Cambridge, MA 02138, USA; joseph.michail@cfa.harvard.edu
[2] Canadian Institute for Theoretical Astrophysics, University of Toronto, 60 Saint George Street, Toronto, ON M5S 3H8, Canada; s.fellenberg@utoronto.ca
[3] Max Planck Institute for Radioastronomy, Auf dem Hügel 69, Bonn, Germany
[4] Department of Physics, McGill University, 3600 Rue University, Montréal, QC H3A 2T8, Canada
[5] Trottier Space Institute at McGill, 3550 Rue University, Montréal, QC H3A 2A7, Canada
[6] East Asian Observatory, 660 North A'ohoku Place, Hilo, HI 96720, USA
[7] Academia Sinica Institute of Astronomy and Astrophysics, 645 North A'ohoku Place, Hilo, HI 96720, USA
[8] Department of Physics and Astronomy, University of Hawaii at Manoa, 2505 Correa Road, Honolulu, HI 96822, USA
[9] Anton Pannekoek Institute for Astronomy, University of Amsterdam, Science Park 904, 1098 XH Amsterdam, The Netherlands
[10] Gravitation and Astroparticle Physics Amsterdam Institute, University of Amsterdam, Science Park 904, 1098 XH 195 196 Amsterdam, The Netherlands
[11] Institute of Astronomy, University of Cambridge, Madingley Road, Cambridge CB3 0HA, UK
[12] Dunlap Institute for Astronomy and Astrophysics, University of Toronto, 50 Saint George Street, Toronto, ON M5S 3H4, Canada
[13] Department of Physics, University of Toronto, 60 Saint George Street, Toronto, ON M5S 1A7, Canada
[14] University of Maryland, College Park, MD 20742, USA
Received 2026 February 6; revised 2026 March 24; accepted 2026 April 8; published 2026 May 12

Abstract

MAXI J1744−294 (MAXI J1477), likely a low-mass X-ray binary system, is a Galactic center transient source, detected at radio and X-ray wavelengths, located approximately 19″ southeast of Sgr A*. We report the first detection of its variable linear polarization in four epochs spanning 2025 April 4–9. The normalized 33 and 43 GHz Stokes parameters q and u over the four epochs imply a common Faraday rotation screen with a rotation measure (RM) $=-63606^{+844}_{-861}$ radians m^{-2}, the third largest RM detected within the Galaxy. The RM is consistent with that of the Galactic center magnetar PSR J1745−2900, giving the first direct evidence that MAXI J1744 lies within the Galactic center region, is bound to Sgr A*, and therefore is part of the nuclear star cluster. The uniformity in the Galactic center Faraday screen suggests that Sgr A*'s $\approx -10^5$ radians m^{-2} RM is intrinsic rather than originating from an unrelated line-of-sight source. On 2025 April 6, we detected a secondary polarized component with an additional RM ≈ -6000 radians m^{-2}, which was not seen at any other epoch. Assuming this secondary component primarily cools by synchrotron radiation, the implied local magnetic field strength is ∼15–30 G. In the context of a jetted X-ray binary progenitor, the additional RM screen and magnetic field strength are explainable with a short-lived knot in a putative jet.

Unified Astronomy Thesaurus concepts: Galactic center (565); Polarimetry (1278); Transient sources (1851); Radio interferometry (1346)

1. Introduction

MAXI J1744−294 (MAXI J1744) is the most recent Galactic center (GC) transient source. It was discovered in X-rays by the Monitor of All-sky X-ray Image (MAXI) on board the International Space Station in early 2025 January (Y. Kudo et al. 2025). Given the large positional uncertainty of the MAXI instrument, follow-up observations by the X-ray NinjaSat satellite were consistent with a new transient, rebrightening events from two X-ray sources near Sgr A* previously in outburst, or potentially Sgr A* itself (Y. Kudo et al. 2025; M. Nakajima et al. 2025; S. Watanabe et al. 2025). Subsequent Neil Gehrels Swift Observatory (Swift) monitoring (C. O. Heinke et al. 2025), with its higher angular resolution, revealed a separate source southeast of Sgr A*. Archival X-ray analysis later indicated that MAXI J1744 is associated with the previously known transient Swift J174540.2−290037, first discovered in outburst in 2016 May with Swift (N. Degenaar et al. 2016a, 2016b; S. Mandel et al. 2025a, 2026). K. Mori et al. (2019) presented a comprehensive analysis of its X-ray (Chandra and NuSTAR) properties during the 2016 outburst. No published radio limits exist during the 2016 May outburst, and the X-ray flux decayed by 2016 mid-July. By coincidence, the National Radio Astronomy Observatory's Karl G. Jansky Very Large Array (VLA) Sky Survey (VLASS; M. Lacy et al. 2020) made a pilot observation near Sgr A* on 2016 August 13. Data retrieved from the VLASS archive show no discernible source at the Swift J174540.2−290037 location and place a 3σ upper limit of ∼1 mJy beam^{-1} at 3 GHz on the source's radio emission on that date.

S. Mandel et al. (2025a) provided a comprehensive multi-wavelength study of the 2025 outburst, focusing on X-ray light

[15] NSF Astronomy and Astrophysics Postdoctoral Fellow.
[16] Feodor Lynen Fellow.
[17] Deceased after manuscript submission, 2026 February.

Original content from this work may be used under the terms of the Creative Commons Attribution 4.0 licence. Any further distribution of this work must maintain attribution to the author(s) and the title of the work, journal citation and DOI.

Table 1
VLA Observing Parameters for the Data Used in This Analysis

Date	On-source Time (hr)	Band	Synthesized Beam arcsec × arcsec (deg)
2025 Apr 4	3.39	*Q*	2.57 × 1.40 (−4.33)
2025 Apr 6	3.75	Ka	3.93 × 1.81 (0.80)
2025 Apr 7	3.39	*Q*	3.19 × 1.59 (−3.02)
2025 Apr 9	3.75	Ka	3.82 × 1.83 (−1.26)

curves and spectra. The study includes NuSTAR, XMM-Newton, and Swift spectral observations and modeling, which were best fit by a compound blackbody accretion disk and a power law, signaling a low-mass X-ray binary source in a soft state. Additional X-ray follow-up included XRISM (S. Mandel et al. 2025b), Einstein Probe (Y. Wang et al. 2025), Chandra (S. Mandel et al. 2025c), and NICER (2025 March; G. K. Jaisawal et al. 2025). Furthermore, the IXPE X-ray polarimeter placed a 3σ upper limit of 1.3% on the linear polarization across the 2–8 keV band (L. Marra et al. 2026). S. Mandel et al. (2025a) did not detect a near-infrared counterpart in Keck continuum ($\lambda \approx 2.12$ and 2.27 μm) or in Brγ data.

The first 2025 detection of a radio counterpart of MAXI J1744 was on 2025 January 25 by MeerKAT (N. Grollimund et al. 2025) at *L* band (≈1.28 GHz) as a flux excess compared to previous images of ≈110 ± 50 mJy embedded in the extended GC emission. J. M. Michail et al. (2025) detected MAXI J1744 at 33 and 43 GHz with the VLA on 2025 April 4, finding that the source's total intensity varied by a factor of ≈2–3 over subsequent observations on 2025 April 6, 7, and 9. Using full-track VLA observations of Sgr A* in 2024 April, J. M. Michail et al. (2025) placed $3\sigma \approx 4$ mJy beam^{-1} flux limits at 22, 33, and 44 GHz on MAXI J1744's quiescent radio flux prior to the 2025 January outburst. The 2025 VLA observations also showed that the radio spectral index changed significantly over these few days. This change was accompanied by an increased X-ray hardness and hard X-ray (7.2–50 keV) count rate as probed by NuSTAR (S. Mandel et al. 2025a).

This paper presents the first detection of MAXI J1744's radio polarization and rotation measure (RM) with the VLA at 33 and 43 GHz in 2025 April. These data were taken as part of our ongoing multiwavelength monitoring of the variability of Sgr A* and its surroundings (T. Roychowdhury et al. 2025; S. D. von Fellenberg et al. 2025; J. M. Michail et al. 2026). Section 2 describes the calibration and imaging of the radio data. Section 3 analyzes the polarization properties and evolution and models the normalized Stokes *q* and *u* spectra to reveal the third-largest RM from a Galactic source. Section 4 discusses the results, and Section 5 summarizes our work and presents our conclusions.

2. VLA Data and Calibration

2.1. Observing Setup and Calibration

We obtained four full-track D-configuration observations of Sgr A* and its environs during 2025 April (project ID 25A-314, PI: J. M. Michail) as part of a multiwavelength campaign targeting Sgr A* and spanning radio through X-ray frequencies. Table 1 describes the observational parameters for the datasets used in this analysis. The observations used the 3 bit setup, providing full polarimetric products over 63 spectral windows (SPWs), each SPW composed of 64 2 MHz-wide channels. This gave 8 GHz of contiguous bandwidth between 29.1 and 37.0 GHz (*Ka* band, 33 GHz) or 40.1–48.0 GHz (*Q* band, 43 GHz).

Standard high-frequency observational setups were completed, including regular pointing calibration required above 15 GHz. The Stokes *I* data were processed through the default VLA pipeline in CASA 6.4.1 (CASA Team et al. 2022), and further manual processing to calibrate the polarization products followed the standard VLA polarization recipe.[18] We used J1331+3030 as the flux and absolute polarization-angle calibrator, J1733−1304 as the bandpass and instrumental polarization calibrator, and J1744−3116 as the complex gain calibrator. After calibration, data on Sgr A* underwent manual data flagging and two rounds of phase self-calibration with 3 s solution intervals. Phase self-calibration on baselines $\geqslant 30k\lambda$ assumed a point source at the phase center. The data were imaged on all baselines, and the model components were used for phase self-calibration. Before imaging, we recomputed the statistical weights on the visibility data with `statwt`. Appendix A defines the polarization conventions used in this paper, and Appendix B gives estimates of the residual instrumental polarization.

2.2. Imaging and Aperture Photometry

Two `TCLEAN` imaging runs were needed to create observation-averaged full-polarization spectral cubes of the region surrounding Sgr A*. The first run imaged the Stokes *I* and *V* planes (`specmode = 'cube'`, `stokes = 'IV'`) at 32 MHz spectral resolution (`width = '32MHz'`). The `auto-multi-thresh` automatic masking algorithm (A. A. Kepley et al. 2020) was required because of the extended Minispiral emission in Stokes *I*. Stokes *V* was also imaged as a diagnostic of potential calibration- or antenna-based corruptions (such as beam squint). The second run imaged the Stokes *Q* and *U* planes (`stokes = 'QU'`) with a manual mask composed of two circular, 5″ radius masks centered on Sgr A* and MAXI J1744.

The *IQUV* images for each observation epoch used a common restoring beam (`restoringbeam = 'common'`) as listed in Table 1. The cubes were noninteractively CLEANed with the multiscale deconvolver, `scales = [0, 5, 15] pixels`, and a 3σ rms stopping criterion. Additional parameters were Briggs weighting with `robust = 0.5`, imaging limited to projected baselines $\geqslant 10k\lambda$ to suppress emission with angular sizes $\geqslant 21''$, and a per-plane primary-beam correction (`pbcor = True`). The final 43 GHz data used a pixel size of 0.″24 and an image size of 432 pixels (1.′73), and the 33 GHz data used 0.″32 pixels with an image size of 450 pixels (2.′40). The primary-beam-corrected cubes were exported from CASA format into FITS cubes for further analysis. The left and central panels of Figure 1 show single-epoch 33 GHz images of Sgr A* in Stokes *I* (total intensity) and polarized intensity (*PI*).

Stokes *I*, *Q*, and *U* values for Sgr A* and MAXI J1744 were measured from aperture photometry with the `photutils` package (Astropy Collaboration et al. 2013, 2018, 2022). The chosen aperture was elliptical with the same position angle as the synthesized beam and 1.25× the radius (Table 1). The aperture centers were determined from the *PI* image (e.g., the

[18] https://casaguides.nrao.edu/index.php/CASA_Guides:Polarization_Calibration_based_on_CASA_pipeline_standard_reduction:_The_radio_galaxy_3C75-CASA6.5.4

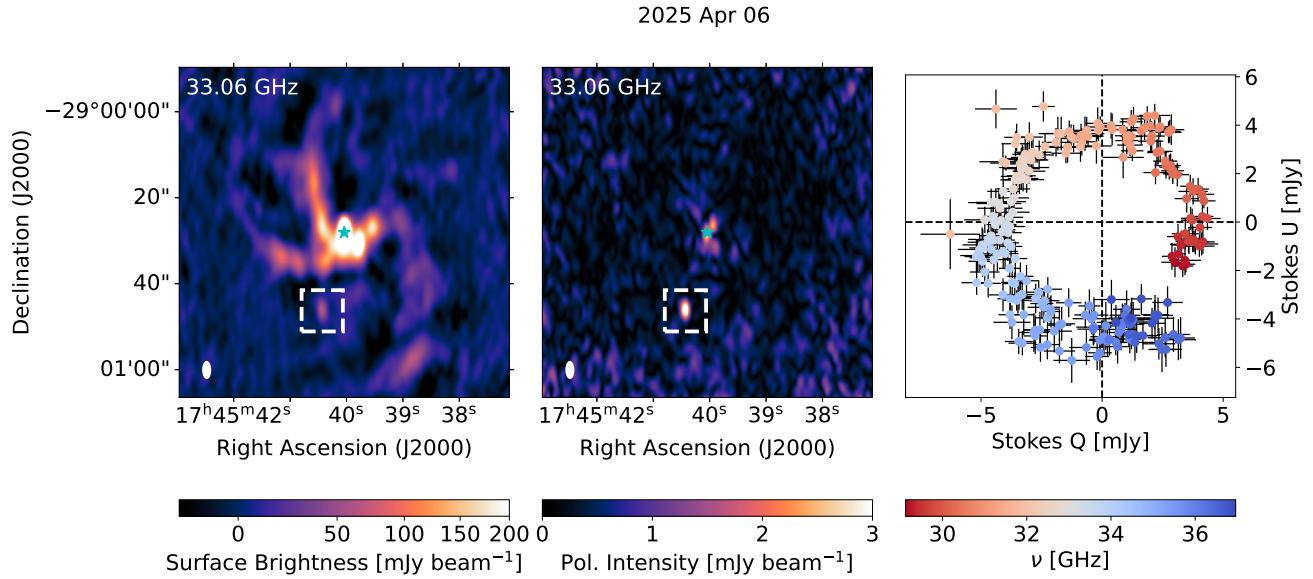

Figure 1. 33 GHz images of Sgr A* and MAXI J1744 on 2025 April 6. Left: Stokes *I* image. Sgr A* is marked with a cyan star, and MAXI J1744 is marked with a white dashed box. The synthesized beam is shown in the lower left corner. Center: linearly polarized flux (*PI*) image. The markings are as in the left panel. Right: Stokes *U* vs. *Q* of MAXI J1744. The colored points correspond to frequency as indicated in the color bar. The counterclockwise orientation of the loop with increasing frequency corresponds to a negative RM.

central panel of Figure 1) at each epoch. *PI* is preferred over the individual Stokes parameters because it has no large-scale component (unlike Stokes *I*), and *PI* is positive definite, which is not necessarily true for Stokes *Q* and *U*. Both properties make the centroiding procedure more accurate. The single aperture location per observation assumes that the total and polarized intensities are colocated (i.e., no core shift nor extended component), which is reasonable given the large restoring beams. On 2025 April 6, the Stokes *I* spectrum of MAXI J1744 was dimmer by ∼10 mJy in a single baseband covering 31–33 GHz. This shift also appeared in Sgr A*'s spectrum and in the Stokes *I* spectra of J1733−1304 and J1744−3116, consistent with a flux bootstrapping calibration issue. This issue was limited to Stokes *I* with no similar issues being detected in MAXI J1744's Stokes *Q* and *U* spectra. Moreover, neither the instrumental polarization solutions nor Stokes *Q* and *U* spectra for J1733−1304 or J1744−3116, produced using the same methods, showed any systematic variations in the 31–33 GHz linear polarization on 2025 April 6. Appendix C describes how the *I* flux scaling for 2025 April 6 was corrected. The noise estimates on the measured Stokes parameters were calculated using the standard deviation in a nearby region which does not contain any significant sources or emission.

This paper's key results are based on normalized Stokes parameters (Stokes $q \equiv Q/I$ and $u \equiv U/I$), which remove the Stokes *I* spectral dependence from Stokes *Q* and *U* that may otherwise cause artifacts in the derived polarization properties if not accounted for (M. A. Brentjens & A. G. de Bruyn 2005).

3. Rotation Measure and Polarization Properties

3.1. Total Intensity and Polarization Variability

The right panel of Figure 1 shows a Stokes *U* versus *Q* plot for the Ka-band observation on 2025 April 6; the loop is counterclockwise oriented with increasing frequency, exhibiting the presence of an intrinsic, negative RM across the band. Figure 2 shows the normalized Stokes parameter spectra for each epoch across the full ∼8 GHz bandwidth. There are correlated spectral changes in the normalized Stokes parameters between each epoch, consistent with variable polarization properties on a ∼few day cadence. To quantify the variability of the linear polarization, we calculated the band-averaged debiased *PI* and polarization percentages for each observation, which are listed in Table 2. (These quantities are defined in Appendix A.) The linear polarization fractions of MAXI J1744 on 2025 April 7 and 9 were approximately 3 times lower than on 2025 April 4 and 6, whereas the *PI* decreased only by a factor of ∼2 over the same period. The larger change in the polarization percent was exacerbated by the increasing flux density of ∼40% at 43 GHz and ∼25% at 33 GHz.[19]

Changes in the flux density were also commensurate with increases of the in-band spectral index (α; $F_\nu \propto \nu^\alpha$), calculated from the Stokes *I* spectra (Section 2) rebinned to 256 MHz resolution. We excluded $\nu \geqslant 47.5$ GHz from the fitting on 2025 April 4 and 7, as residual spectral roll-off is present in the spectra of MAXI J1744 and Sgr A*. There was a statistically significant hardening, i.e., an increase in α, in the radio spectra across the 33 GHz ($\Delta\alpha_{33\,\mathrm{GHz}} = 0.84 \pm 0.13$) and 43 GHz bands ($\Delta\alpha_{43\,\mathrm{GHz}} = 0.96 \pm 0.16$). The changes in the spectral index across these two bands are statistically consistent, suggesting a single event or component was responsible the change in Stokes *I*.

3.2. Stokes q and u Spectral Fitting

3.2.1. Per-epoch Modeling

We utilized the `RM-Tools` (C. R. Purcell et al. 2020)[20] package to directly fit the Stokes *q* and *u* spectra for each observation. In contrast to fitting only the changes in the

[19] There is a typo in the 33 GHz flux density listed by J. M. Michail et al. (2025) on 2025 April 6, which initially showed a more drastic increase in the 33 GHz band flux density.

[20] https://github.com/CIRADA-Tools/RM-Tools

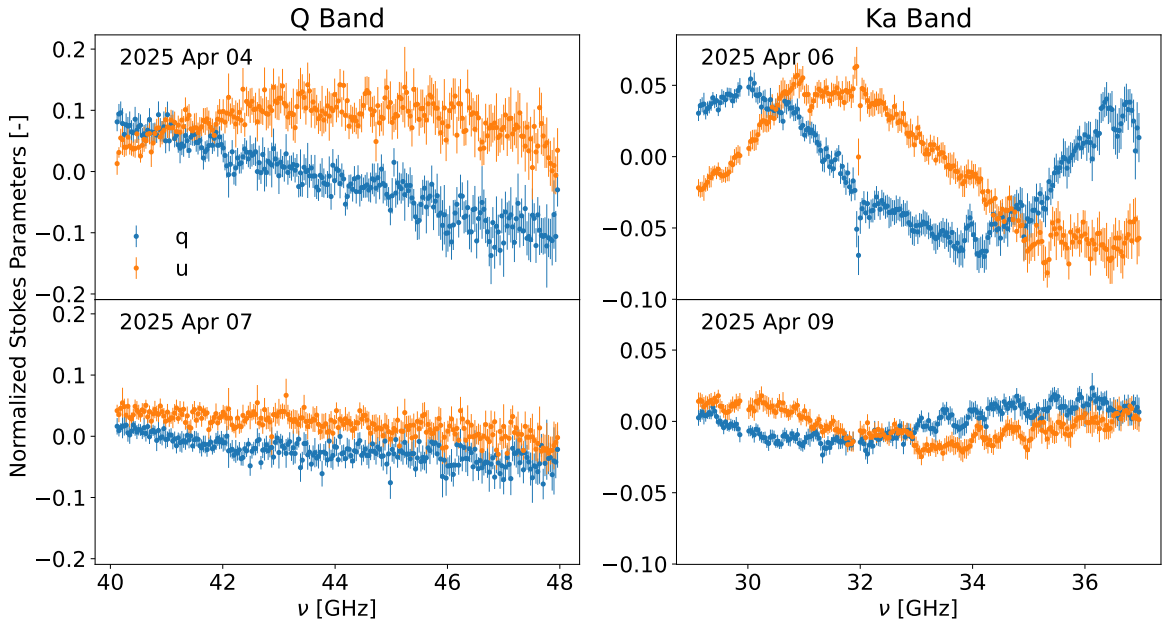

Figure 2. Normalized polarization parameters q (blue) and u (orange) of MAXI J1744 for each observation at 32 MHz spectral resolution.

Table 2
Total Intensity and Band-averaged Linear Polarization Intensity and Percentage of MAXI J1744

Date	Stokes I [a] (mJy)	α	PI (mJy)	Polarization (%)
		33 GHz		
2025 Apr 6	74.9 ± 0.6	-1.58 ± 0.12	4.03 ± 0.03	5.45 ± 0.07
2025 Apr 9	94.6 ± 0.4	-0.74 ± 0.06	1.27 ± 0.03	1.34 ± 0.03
		43 GHz		
2025 Apr 4	53.4 ± 0.4	0.08 ± 0.13	5.47 ± 0.07	10.12 ± 0.13
2025 Apr 7	73.9 ± 0.3	1.04 ± 0.09	2.74 ± 0.06	3.59 ± 0.08

Note.
[a] Listed flux densities are evaluated at 33 and 43 GHz for the Ka and Q bands, respectively. The in-band spectral index α is defined by $F_\nu \propto \nu^\alpha$.

electric vector position angle (EVPA), this removes $n\pi$ ambiguities. Details about `RM-Tools`, the models used, and per-epoch fits are in Appendix D. In short, we fit each epoch with two models: (1) a single polarized component with one external Faraday screen, and (2) two polarized components (within the same beam) with two separate Faraday screens. The polarization properties of MAXI J1744 are best represented by a single component on 2025 April 4, 7, and 9. However, two separate polarized components are significantly favored on 2025 April 6. The two-component model on April 6 is still preferred even when excluding the 31–33 GHz data because of the flux-scaling issue (Section 2.2, Appendix C). This test eliminates the possibility of a data-quality or systematic issue explaining the second component. Figure 3 shows the single- and double-component Stokes q and u model fits on this date, clearly demonstrating the need for a secondary component.

The `RM-Tools` fits show a persistent Faraday screen with RM $\approx -63{,}000$ radians m^{-2}, consistent with the intervening GC screen as probed by the GC magnetar PSR J1745−2900 (e.g., R. P. Eatough et al. 2013; G. Desvignes et al. 2018), yielding the first direct evidence that MAXI J1744 lies behind the GC screen and is most likely bound to Sgr A*. Additionally, the 2025 April 6 second component shows that the more highly polarized component has a higher Faraday depth, suggestive of a Faraday screen local to MAXI J1744's environment.

3.2.2. Joint-epoch Modeling

The consistent value of the GC-associated Faraday screen in the per-epoch fitting motivates a joint fit to all four epochs with a more sophisticated model. A schematic diagram of this setup is shown in Figure 4. Using the results from the individual epoch fitting, we assume MAXI J1744 is best described on 2025 April 4, 7, and 9 by a single component with fixed $\phi_{\rm GC}$ and other parameters varying by date:

$$p_{\rm Apr\{4,7,9\}}(\lambda) = p_{0,\rm Apr\{4,7,9\}}\, e^{2i(\psi_{0,\rm Apr\{4,7,9\}} + \phi_{\rm GC}\lambda^2)}, \quad (1)$$

where $p_{0,\rm Apr\{4,7,9\}}$ and $\psi_{0,\rm Apr\{4,7,9\}}$ are the intrinsic polarization fractions and EVPA on each of the days, respectively, and $\phi_{\rm GC}$ is the Faraday depth of the invariant GC screen.

On 2025 April 6, we account for a secondary component with an additional, local Faraday screen ($\phi_{\rm local}$), which also passes through the GC screen:

$$p_{\rm Apr\,6}(\lambda) = p_{0,\rm Apr\,6,1} e^{2i(\psi_{0,\rm Apr6,1} + \phi_{\rm GC}\lambda^2)} + p_{0,\rm Apr\,6,2}\, e^{2i(\psi_{0,\rm Apr6,2} + (\phi_{\rm GC}+\phi_{\rm local})\lambda^2)}. \quad (2)$$

Here $p_{0,\rm Apr\,6}$ and $\psi_{0,\rm Apr6}$ have the same meaning as in Equation (1), only for 2025 April 6. The "1" and "2" subscripts denote components that are affected only by the GC Faraday screen and by both the local and GC Faraday screens, respectively. $\phi_{\rm GC}$ is common to all observations. The joint fit had to be completed outside of `RM-Tools`, which is currently unable to do joint-epoch fitting. However, our implementation used the same underlying fitting code (`dynesty`; S. Koposov et al. 2022) and cost function as `RM-Tools` for consistency. The best-fit joint-modeling parameters are shown in Table 3.

While our VLA observations detected the secondary polarized component on 2025 April 6, the observing frequency

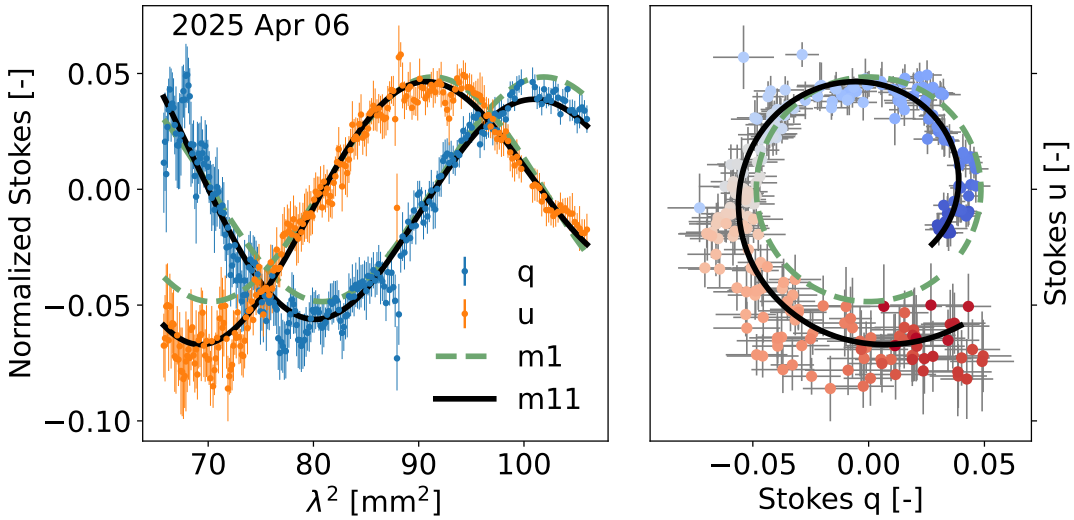

Figure 3. Normalized Stokes q and u parameters of MAXI J1744 on the 2025 April 6 epoch compared with the best-fit `m1` (dashed light green lines; single component) and `m11` (solid black lines; double component) models. Appendix D gives more details about the models. Left: Stokes q and u spectra. Right: Stokes q vs. u plot. The data point colors correspond to the observing frequency, matching the color scheme in Figure 1.

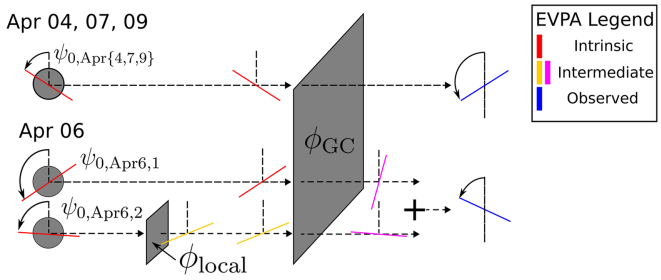

Figure 4. Schematic setup of the joint polarization fit among all four VLA epochs. The first, third, and final epochs are affected only by the single GC Faraday screen (ϕ_{GC}) whereas one of the two components in the second epoch has an additional secondary Faraday screen (ϕ_{local}). Intrinsic polarization angles for each day and component are denoted in red, while the measured polarization angles are in blue. Intermediate (unobserved) polarization angles are shown in yellow and magenta. "+" denotes that the sum of the two components gave the observed linear polarization on 2025 April 6. Physical scales are not accurately represented.

was too high to resolve any polarized substructures in the localized RM screen. Such polarized substructure is normally detected using RM synthesis (e.g., S. P. O'Sullivan et al. 2012). However, J. M. Dickey et al. (2019) showed the FWHM of the recovered RM synthesis spectrum is FWHM $= 3.8/(\lambda^2_{\mathrm{max}} - \lambda^2_{\mathrm{min}})$. For the 33 GHz VLA data, FWHM $\approx 100{,}000$ radians m$^{-2} \gg |\phi_2|$, rendering this impossible with the current data. Continued monitoring of MAXI J1744's polarized properties should be concentrated at lower frequencies, where polarized substructures can be resolved in the RM synthesis spectrum. However, such lower-frequency observations will contend with bandwidth depolarization from the GC Faraday screen, thus requiring high frequency resolution (e.g., G. C. Bower et al. 1999).

4. Discussion

4.1. Temporal Evolution of the Primary Polarized Component

Table 3 lists the joint-fit parameters for the "primary" polarization component (i.e., the component affected only by the GC Faraday screen) and the "secondary" component (i.e., the component with an additional, local Faraday screen). The

Table 3
Joint Model Best-fit Parameters

Parameter	Prior	Posterior (68% CI)[a]
ϕ_{GC} [radians m^{-2}]	$\mathcal{U}[-110,\,000,\,0]$[b]	$-63,\,606^{+844}_{-861}$
$p_{0,\mathrm{Apr\ 4}}$ [%]	$\mathcal{U}[0,\,100]$	$9.84^{+0.16}_{-0.16}$
$p_{0,\mathrm{Apr\ 6,1}}$ [%]	$\mathcal{U}[0,\,100]$	$8.12^{+5.50}_{-2.82}$
$p_{0,\mathrm{Apr\ 7}}$ [%]	$\mathcal{U}[0,\,100]$	$3.63^{+0.11}_{-0.11}$
$p_{0,\mathrm{Apr\ 9}}$ [%]	$\mathcal{U}[0,\,100]$	$1.54^{+0.04}_{-0.04}$
$\psi_{0,\mathrm{Apr\ 4}}$ [deg]	$\mathcal{U}[0,\,180]$[c]	$39.75^{+2.44}_{-2.38}$
$\psi_{0,\mathrm{Apr\ 6,1}}$ [deg]	$\mathcal{U}[0,\,180]$	$79.95^{+6.11}_{-7.69}$
$\psi_{0,\mathrm{Apr\ 7}}$ [deg]	$\mathcal{U}[0,\,180]$	$61.94^{+2.54}_{-2.56}$
$\psi_{0,\mathrm{Apr\ 9}}$ [deg]	$\mathcal{U}[0,\,180]$	$62.13^{+4.32}_{-4.25}$
ϕ_{local} [radians m^{-2}]	$\mathcal{U}[-110\,000,\,0]$	-6224^{+2119}_{-2482}
$p_{0,\mathrm{Apr\ 6,2}}$ [%]	$\mathcal{U}[0,\,100]$	$11.42^{+5.67}_{-3.19}$
$\psi_{0,\mathrm{Apr\ 6,2}}$ [deg]	$\mathcal{U}[0,\,180]$	$33.15^{+11.99}_{-10.37}$

Notes.
The goodness-of-fit measures for this fit are chi-squared over the degrees of freedom (DOF) $\chi^2/\mathrm{DOF} = 1161.35/1933$, the Bayesian information criterion (BIC) $= -10{,}583.26$, and ln evidence $= 5277.68 \pm 0.33$.
[a] The 68% credible interval (CI).
[b] $\mathcal{U}[a, b]$ is a uniform prior on the inclusive interval $[a, b]$.
[c] Priors on ψ_0 are periodic such that $\psi_0 = 180° + n° = n°$.

primary component's intrinsic linear polarization fraction exhibited a steady decrease over the four epochs, while the intrinsic EVPA changes were more complicated. Between 2025 April 4 and April 6, the intrinsic EVPA swung by $\approx$40° before shifting back by $\approx$10° between April 6 and April 7. It then stabilized through April 9, despite being measured at different frequencies. The trends in the polarization coincide with trends in the spectral index (Table 2): the intrinsic linear polarization decreased as the spectral index hardened and the flux density increased.

In jetted sources, spectral hardening is typically interpreted as an increase in the optical depth of the jet, which can lower both the observed flux density (R. D. Blandford & A. Königl 1979) and the linear polarization (M. S. Longair 2011). The measured anticorrelation in the radio spectral index and intrinsic polarization is consistent with an increase in the jet's

optical depth. However, the jet did not enter a fully optically thick regime, as $\alpha \neq 2.5$ (J. J. Condon & S. M. Ransom 2016), nor did the intrinsic EVPA exhibit the expected $\sim 90^\circ$ rotation (M. S. Longair 2011). The flux density did not follow the expected trend, as it increased despite the hardened radio spectrum. Observations of other jetted sources at ~daily cadence (e.g., D. C. Hannikainen et al. 2000) typically show an anticorrelation in the spectral index and flux density during individual flaring events, consistent with an increasing optical depth. However, C. Brocksopp et al. (2013) detected one instance where a hardened radio spectrum corresponded to an increased flux density and linear polarization at 5.5 and 9 GHz, which they argued can be explained by a forming compact jet. The overall evolution of MAXI J1744's radio polarization over these four epochs appears consistent with the formation and/or evolution of a compact jet and is also compatible with the lack of detectable X-ray polarization by IXPE, which observed between 2025 April 5 and April 8 (L. Marra et al. 2026), although in other stellar-mass black hole binaries, the X-ray polarization may instead trace the accretion disk and/or corona rather than the jet (N. Rodriguez Cavero 2024). Yet, ~minute timescale radio monitoring of V404 Cyg (A. K. Hughes et al. 2023) found uncorrelated variability in the flux density and linear polarization evolution over ~4 hr. Their results suggest changes in the flux density and polarization may be caused by more complicated, multicomponent emission rather than a single emitting zone. The data presented here also suggest MAXI J1744 contains additional components (beyond the second polarized component on 2025 April 6) that are spatially, spectrally, and polarimetrically unresolved by our observations. Moreover, ~daily X-ray monitoring with NuSTAR, NICER, Swift (S. Mandel et al. 2025a), and IXPE (L. Marra et al. 2026) show that the X-ray flux peaked just before 2025 April 1 and around the time of these radio observations, indicating that the radio polarization evolves within a broader phase of multiwavelength variability. Given the potentially complicated and unresolved structure of this source, we cannot necessarily correlate changes in the intrinsic EVPA with substructure in the source, e.g., the jet's position angle, consistent with high-resolution observations of V404 Cyg with the Very Long Baseline Array (J. C. A. Miller-Jones et al. 2019).

4.2. A Knot Explanation for the Secondary Polarized Component

The secondary component was slightly more polarized than the primary component on 2025 April 6 as probed by the median posterior values in Table 3. However, the 68% CIs for the two components significantly overlap, suggesting that the difference in the intrinsic polarization levels is not significant. The localized Faraday screen with RM ≈ -6200 radians m^{-2} reveals the line-of-sight magnetic field is oriented away from Earth (i.e., in the same direction as the GC screen).

The large RM value in this secondary Faraday screen suggests a strong magnetic field, potentially within a jet, and/or a magnetic field largely along the line of sight. We take two approaches to test if this is a viable explanation. First, assuming this component cools only via synchrotron emission allows for an estimate of the (total) magnetic field strength. Using standard synchrotron relationships (G. B. Rybicki & A. P. Lightman 1986; J. J. Condon & S. M. Ransom 2016), and assuming an isotropic pitch angle, the estimated local magnetic field strength $B_{\rm local}$ and synchrotron cooling timescale $t_{\rm cool}$ are related by

$$B_{\rm local} = 2\left(\frac{t_{\rm cool}}{1\ {\rm yr}}\right)^{-2/3}\left(\frac{\nu}{1\ {\rm GHz}}\right)^{-1/3}\ {\rm G}. \quad (3)$$

If $t_{\rm cool} = 1$ day, estimated from the secondary component appearing on 2025 April 6 and disappearing on 2025 April 7, and $\nu = 43$ GHz, $B_{\rm local} \approx 30$ G. A cooling timescale of 1 day is a lower bound on the true value, however, as this secondary component could have formed anytime after the end of the first observation (2025 April 4). If $t_{\rm cool} = 3$ days, $B_{\rm local} \approx 15$ G. Therefore, the synchrotron estimate is consistent with a local magnetic field strength of 15–30 G. The cooling-timescale-based estimate does not account for higher-energy electrons that cool to the radio and emit (lengthening the required cooling time for the knot) and ignores any adiabatic cooling or expansion of the knot moving through the jet opening angle (biasing the magnetic field strength estimate to higher values).

The second estimate comes from the analytic model developed for MAXI J1820+070 (A. A. Zdziarski et al. 2022) and used by A. K. Hughes et al. (2023) for the 2015 radio outburst of V404 Cygni. This model estimates the magnetic-field strength and electron number density (n_e) in a steady-state, conical jet. Following A. K. Hughes et al. (2023), we adopt the fiducial jet parameters from A. A. Zdziarski et al. (2022) for MAXI J1820+070 in this computation. At 33 GHz, we estimate a total magnetic field strength ≈ 20 G and $n_e \approx 6100\ {\rm cm}^{-3}$. Assuming the localized Faraday screen can be described by a one-zone model, the RM is related to the line-of-sight magnetic field strength ($B_\parallel$), electron number density, and thickness of the screen (dl) by ${\rm RM} = n_e B_\parallel dl$. With $|{\rm RM}| = 6223$ radians m^{-2}, assuming $B_\parallel = 0.5B \approx 10$ G, and $n_e = 6100\ {\rm cm}^{-3}$, gives $dl \approx 0.03$ au. A. K. Hughes et al. (2023) derived a screen thickness of 0.06 au for V404 Cygni, assuming the observed RM was produced by a radio jet.

The two magnetic field strength estimates and the Faraday screen depth are broadly consistent with the physical conditions in a polarized radio jet. These results suggest the secondary component formed as a short-lived knot within a jet and cooled via synchrotron radiation within the jet's strong magnetic field. Depending on the optical depth of the potential knot, the intrinsic EVPA may trace the jet's orientation.

4.3. Radial Profile of the Rotation Measure in the Central Parsec

Before this work, only two objects in the central parsec of the Galaxy had measured RM values: Sgr A* and the GC magnetar PSR J1745−2900 with RM $\approx -5 \times 10^5$ (e.g., G. C. Bower et al. 2003; D. P. Marrone et al. 2007; G. C. Bower et al. 2018) and $\approx -(6\text{–}7) \times 10^4$ radians m^{-2} (R. P. Eatough et al. 2013; G. Desvignes et al. 2018), respectively. Farther out, however, the Galaxy within the inner few degrees has lower and/or positive RMs as probed by pulsars (within a projected distance of ~30 pc of Sgr A*; F. Abbate et al. 2023) and background quasars (S. Roy et al. 2008), suggesting a variable and complicated magnetic configuration. Attempts to explain this large-to-small-scale change in the RM include local conditions (i.e., higher magnetic field and particle densities in the GC; R. P. Eatough et al. 2013), Galactic structures (i.e., spiral arms or the Galactic

bar; S. Roy et al. 2008), or intervening line-of-sight sources (such as H II regions; E. Sicheneder & J. Dexter 2017). Moreover, the measured RMs of Sgr A* and PSR J1745−2900 appeared to temporally vary (e.g., G. C. Bower et al. 2018; G. Desvignes et al. 2018). D. P. Marrone et al. (2006) showed that the RM can be used to probe the accretion rate of Sgr A*. It is therefore crucial to understand the line-of-sight RM structure because treating an external RM as intrinsic to Sgr A* would affect the accretion rate measurement using this method.

R. P. Eatough et al. (2013) used measurements of the magnetic field ($B(r)$) and particle densities ($n(r)$) at arcminute to degree scales in the GC to argue that the observed RM of PSR J1745−2900 originates from a Faraday screen on ∼10 pc scales. They assumed that the magnetic field strength and particle density both vary as r^{-1}, yielding $\mathrm{RM_{screen}} = B(r)n(r)r \propto r^{-1}$. This implies the GC screen substantially contributes to Sgr A*'s measured RM, as $\mathrm{RM_{screen}}$ increases toward Sgr A*. However, without a suitable secondary source, the local RM profile of the GC screen could not be tested.

MAXI J1744 gives us this opportunity, as it is now the source with the largest projected radial separation from Sgr A* within the central parsec (projected radius of 18.″8 corresponding to ∼0.75 pc at a distance of 8.178 kpc; GRAVITY Collaboration et al. 2019). Using the GC magnetar RM (−66,960 ± 50 radians $\mathrm{m^{-2}}$ at projected radius of ≈3″; R. P. Eatough et al. 2013) as an anchor point with MAXI J1744's measured value (−63,606 ± 850 radians $\mathrm{m^{-2}}$) yields RM $\propto r^{-0.03 \pm 0.01}$ within the central parsec, which is extremely shallow and consistent with a flat RM screen on a scale of ∼ 1 pc. If no abrupt changes in the RM profile exist and the RM screen is azimuthally symmetric, our results support a similarly strong foreground RM ≈ −(6–7) × 10^4 radians $\mathrm{m^{-2}}$ (≈10%) contribution to Sgr A*'s measured RM. Consequently, the majority of Sgr A*'s ≈−5 × 10^5 radians $\mathrm{m^{-2}}$ originates from the accretion flow rather than from an external source.

However, we cannot ascertain the true origin of the GC Faraday screen. For example, the best-fit ranges of H II region parameters capable of describing the large-scale scattering, dispersion, and Faraday characteristics toward the GC (E. Sicheneder & J. Dexter 2017) result in projected angular sizes of 1′–7′. Because MAXI J1744 lies within this range of projected radii from Sgr A*, our data are insensitive to spatial structures greater than its projected radius (≈0.′3) and cannot rule out or constrain such origins. However, we can eliminate scenarios where the large RM present in the GC is only locally produced given the nearly flat RM profile, e.g., PSR J1745−2900 interacting with nearby ionized gas (F. Yusef-Zadeh et al. 2015).

5. Conclusions and Summary

We have presented the first linear polarization detection of the GC transient MAXI J1744 with 33 and 43 GHz VLA observations in 2025 April. Stokes q and u modeling shows that the linear polarization of MAXI J1744 varied on a ∼daily timescale.

1. There is a persistent Faraday screen with RM = -63606^{+844}_{-861} radians $\mathrm{m^{-2}}$, consistent with the GC Faraday screen probed by the GC magnetar PSR J1745−2900. This measured RM is the first direct evidence that MAXI J1744 resides within the GC instead of in the foreground.
2. There was a secondary polarized component on 2025 April 6 with a localized RM ≈ −6200 radians $\mathrm{m^{-2}}$. This component was absent in polarization data taken before and after this date. Its nature is consistent with a short-lived knot in a putative radio jet with an ≈15–30 G magnetic field.
3. The RMs for MAXI J1744 and PSR J1745−2900 are nearly equal. This supports the notion that most of Sgr A*'s RM (∼-10^5 radians $\mathrm{m^{-2}}$) is intrinsic to the accretion flow rather than an unrelated source along the line of sight.

Acknowledgments

We thank Stéphane Corbel, Noa Grollimund, and Alexander Philippov for discussions about MAXI J1744 early in this paper's analysis, and Shifra Mandel for comments on a draft of this work. We are indebted to the VLA scheduling and operations teams who made these observations possible and to the anonymous referee whose comments helped strengthen this work. The National Radio Astronomy Observatory is a facility of the National Science Foundation operated under cooperative agreement by Associated Universities, Inc. J.M.M is supported by an NSF Astronomy and Astrophysics Postdoctoral Fellowship under award AST-2401752. S.D.v.F. gratefully acknowledges the support of the Alexander von Humboldt Foundation through a Feodor Lynen Fellowship, and thanks CITA for their hospitality and collaboration. Some of the analysis in this paper were conducted on the Smithsonian High Performance Cluster (SI/HPC), Smithsonian Institution.[21] B.R. is supported by the Natural Sciences & Engineering Research Council of Canada (NSERC; funding reference number 568580) and acknowledges support by a grant from the Simons Foundation (MP-SCMPS-00001470). B.R., D.H., N.M.F., Z.S., and M.B. acknowledge support from the Canadian Space Agency under funding number 23JWGO2A01. This research was supported in part by grant NSF PHY-2309135 to the Kavli Institute for Theoretical Physics (KITP). N.M.F. and D.H. acknowledge funding from the Natural Sciences and Engineering Research Council of Canada (NSERC) Discovery Grant program and the Canada Research Chairs (CRC) program. N.M.F. acknowledges funding from the Fondes de Recherche Nature et Technologies (FRQNT) Doctoral research scholarship. N.M.F. and D.H. acknowledge support from the Canadian New Frontiers in Research Fund (NFRF)—Explorations program and the Trottier Space Institute at McGill. The authors acknowledge support from the Centre de recherche en astrophysique du Québec, un regroupement stratégique du FRQNT. S.M. is supported by a European Research Council Synergy Grant "Blackholistic" (grant 10107164). M.B. acknowledges support from the Natural Sciences and Engineering Research Council of Canada's Banting Postdoctoral Fellowship Program (CIHR AWARD BPF 200617-267964).

Facility: VLA.

Software: CASA (CASA Team et al. 2022), astropy (Astropy Collaboration et al. 2013, 2018, 2022), `dynesty` (S. Koposov et al. 2022), `RM-Tools` (C. R. Purcell et al. 2020).

[21] https://doi.org/10.25572/SIHPC

Appendix A
Polarization Conventions

The Stokes parameters I, Q, and U have uncertainties σ_I, σ_Q, and σ_U, respectively. The normalized Stokes parameters q and u therefore have uncertainties σ_q and σ_u:

$$\sigma_q = \sqrt{\left(\frac{1}{I}\sigma_Q\right)^2 + \left(\frac{Q}{I^2}\sigma_I\right)^2}, \text{ and}$$
$$\sigma_u = \sqrt{\left(\frac{1}{I}\sigma_U\right)^2 + \left(\frac{U}{I^2}\sigma_I\right)^2}. \quad \text{(A1)}$$

The debiased linear polarization fraction p_l is defined as

$$p_l = \sqrt{q^2 + u^2 - \sigma_{p_l}^2}, \quad \text{(A2)}$$

where σ_{p_l} is the uncertainty on p_l:

$$\sigma_{p_l} = \frac{\sqrt{q^2\sigma_q^2 + u^2\sigma_u^2}}{\sqrt{q^2 + u^2}}. \quad \text{(A3)}$$

The debiased polarized intensity (PI) and uncertainty on PI are equivalent to Equations (A2) and (A3), respectively, under the change $\{q, u\} \rightarrow \{Q, U\}$. For completeness, the EVPA in radians is defined by

$$\psi = \frac{1}{2}\arctan2\left(\frac{u}{q}\right), \quad \text{(A4)}$$

with the uncertainty on the EVPA σ_ψ:

$$\sigma_\psi = \frac{1}{2}\frac{1}{q^2 + u^2}\sqrt{q^2\sigma_u^2 + u^2\sigma_q^2}, \quad \text{(A5)}$$

where arctan2 places the EVPA in the correct quadrant. Equivalent EVPA relationships using the normal Stokes parameters can again be determined with the change $\{q, u\} \rightarrow \{Q, U\}$.

Appendix B
Estimating Residual Instrumental Polarization

Sgr A* is well known to be linearly unpolarized at radio frequencies (e.g., G. C. Bower et al. 1999, 1999), and, as such, is a useful source to estimate the in-field residual instrumental polarization of the VLA observations given its large Stokes I flux (often $\gtrsim$1.0 Jy). We applied the same aperture extraction methods as in Section 2 to obtain Sgr A*'s Stokes Q and U spectropolarimetry except for centroiding the elliptical aperture in the Stokes I plane instead of PI. The normalized Stokes parameters for Sgr A* are presented in Figure 5. Stokes q and u are centered near zero in the Ka-band observations and do not significantly vary between the two nights; this further confirms that the secondary polarized component observed on 2025 April 6 is not caused by instrumental calibration errors. The normalized Q-band Stokes u parameter is also zero centered in both observations, while the Stokes q parameter is consistently offset by $\approx$+0.005 on 2025 April 4 and 7. This directly points toward an instrument effect as $u \approx 0 \Rightarrow \psi \approx 0$ (Equation (A4)), and, therefore, no RM (RM $\equiv d\psi/d\lambda^2$) for Sgr A*, which lies behind the GC Faraday screen and is known to have a large (sub)millimeter-measured (absolute) RM value in excess of 10^5 radians m^{-2} (e.g., H. B. Liu et al. 2016; G. C. Bower et al. 2018). This "corruption" in Stokes q may be traced back to an imperfect intrinsic polarization calibrator solution in `polcal` and/or an offset in the instrumental polarization leakage terms (see Table 1 of R. J. Sault et al. 1996 for the circularly polarized basis) and consistent with the nominal $\lesssim$0.5% instrumental polarization accuracy for point sources.[22] These spectropolarimetry results suggest residual instrumental polarizations of $\sim$0.2% and $\sim$0.5% in the Ka and Q bands, respectively. Because we followed the VLA setup for polarimetric observations by fixing the absolute polarization angle to a standard source (in this case, J1331+3030), we expect no systematic issues in the EVPA between the Q and Ka bands. MAXI J1744's measured intrinsic linear polarization in the Q band range from 4% to 10% , far exceeding the 0.5% systematic uncertainty, implying that residual instrumental polarization has little effect on the results.

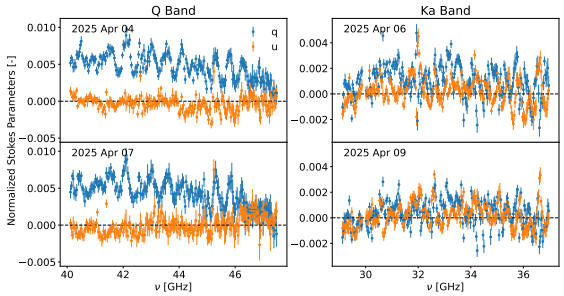

Figure 5. Normalized Stokes parameter spectropolarimetry of Sgr A* for all four observations. Blue and orange show q and u, respectively, as a function of observing frequency. Each panel shows one night's results as labeled.

Appendix C
2025 April 6 Flux Correction

The 31–33 GHz baseband flux density on 2025 April 6 was dimmer by $\approx$10 mJy relative to the rest of the Ka-band observations for MAXI J1744. This issue was also present on the same night for Sgr A*, J1733−1304, and J1744−3116, potentially tracing back to an issue during flux bootstrapping in the VLA pipeline. Attempts to locate the origin of this shift in the calibrated data were unfruitful, as no antenna, baseline, time range, nor correlation appeared inconsistent with the rest of the data. We corrected the flux in the 31–33 GHz frequency range by assuming the spectral energy distribution (SED) of Sgr A* can be described by a power law across the full Ka-band range. We fit the 29.1–31.0 and 33.0–37.0 GHz ranges of Sgr A*'s SED with a power law and determined the residual (model − observed) between 31 and 33 GHz. We then obtain a best-fit linear model to the residuals, which minimizes the measurement noise in the residuals, to calculate the additive offset at each frequency bin at the phase center (i.e., the flux bootstrapping occurs with non-primary-beam-corrected data). To apply corrections to the spectrum of MAXI J1744, we multiplied the flux corrections by the primary-beam response ($\approx$0.85 at the location of the source) and applied these values to the observed spectra for both sources. Figure 6 shows the SEDs of Sgr A* and MAXI J1744 before and after flux correction, which largely recovers the power-law-like SEDs for both sources. After correction, MAXI J1744's spectrum still has lower flux densities near $\approx$30 GHz, but we did not correct these data further. The best-fit power law does not

[22] https://science.nrao.edu/facilities/vla/docs/manuals/oss/performance/polarization

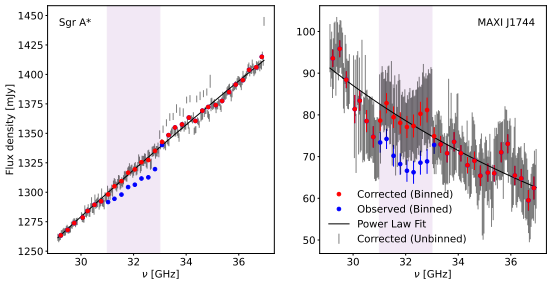

Figure 6. Binned observed (blue) and corrected (red) SEDs of Sgr A* and MAXI J1744, left and right panels, respectively, on 2025 April 6. The native-resolution-corrected SEDs are shown as gray points, and the best-fit power law to the corrected data is shown as a black line. The light purple shaded area denotes the range of frequencies where the correction was applied.

appear to be severely affected by this residual flux bootstrapping issue regardless.

Appendix D
Model Fit Parameters

The most basic polarization model in `RM-Tools` (`m1`) takes the form

$$p_{\mathtt{m1}}(\lambda) = p_0 e^{2i(\psi_0+\phi\lambda^2)}, \tag{D1}$$

where p_0 and ψ_0 are the intrinsic polarization fraction and EVPA, respectively, at a wavelength $\lambda = 0$. ϕ is the Faraday depth of the intervening Faraday screen. This model describes a single polarized component passing through a nonemitting Faraday screen.

We also fit each epoch with a secondary polarization model (`RM-Tools` model `m11`), consisting of two disconnected polarized components within a single beam, each with its own Faraday depth, intrinsic polarization fraction, and intrinsic polarization angle:

$$p_{\mathtt{m11}}(\lambda) = p_{0,1} e^{2i(\psi_{0,1}+\phi_1\lambda^2)} + p_{0,2}\, e^{2i(\psi_{0,2}+\phi_2\lambda^2)}, \tag{D2}$$

where the individual values have the same meaning as above. In this form, $\phi_1 = \phi_{\rm GC}$ and $\phi_2 = \phi_{\rm GC} + \phi_{\rm local}$ (see Equation (2)). In Equations (D1) and (D2) above, the normalized Stokes q and u products are the real and imaginary parts of $p(\lambda)$, respectively.

The best-fit parameters for these two models are listed in Table 4 along with three goodness-of-fit measures calculated by `RM-Tools`: χ^2, the BIC, and the natural logarithm of the Bayesian evidence. `RM-Tools` uses the nested sampler package `dynesty` (S. Koposov et al. 2022) to calculate these measures. For the BIC, only differences are significant, and we adopted the standard $|\Delta\mathrm{BIC}| \equiv |\mathrm{BIC}_2 - \mathrm{BIC}_1| > 10$ value, which signifies model 2 (BIC_2) better represents the data. We chose the better-fitting model as the one preferred by at least two goodness-of-fit parameters. For 2025 April 6, we did the fitting twice for each model: once with all data and once without the 31–33 GHz data. This explicitly ensures that the preferred two-component polarized model on this night is not influenced by the flux-scaling technique explained in Appendix C. In both cases, the two-component model is preferred over the single-component model.

Table 4
Stokes q and u Model Fits for MAXI J1744

Date	Model	Parameter	Prior	Posterior (68% CI)	χ^2/DOF	BIC	ln Evidence
2025 Apr 4	m1[b]	p_0 [%]	$\mathcal{U}[0, 100]$	$9.83^{+0.16}_{-0.15}$	...	...	...
...	...	ϕ [radians m^{-2}]	$\mathcal{U}[-110, 000, 110, 000]$	$-63, 402^{+1856}_{-1705}$	**303.80/488**	**−1954.79**	972.21 ± 0.30
...	...	ψ_0 [°]	$\mathcal{U}[0, 180]$	$39.29^{+4.65}_{-5.15}$	...	...	...
...	m11[a]	$p_{0,1}$ [%]	$\mathcal{U}[0, 100]$	$9.84^{+2.14}_{-1.46}$	...	...	...
...	...	$p_{0,2}$ [%]	$\mathcal{U}[0, 100]$	$3.18^{+3.05}_{-1.42}$	...	...	...
...	...	ϕ_1 [radians m^{-2}]	$\mathcal{U}[-110, 000, 110, 000]$	$-63, 630^{+5719}_{-5400}$	750.88/485	−1960.61	**980.72 ± 0.33**
...	...	ϕ_2 [radians m^{-2}]	$\mathcal{U}[-110, 000, 110, 000]$	$-41, 748^{+29,216}_{-43,667}$	...	...	...
...	...	$\psi_{0,1}$ [deg]	$\mathcal{U}[0, 180]$	$43.03^{+16.02}_{-16.19}$	...	...	...
...	...	$\psi_{0,2}$ [deg]	$\mathcal{U}[0, 180]$	$67.37^{+81.57}_{-42.40}$	...	...	...
2025 Apr 6			All data included in q–u fitting				
...	m1	p_0 [%]	$\mathcal{U}[0, 100]$	$4.85^{+0.05}_{-0.05}$	...	...	...
...	...	ϕ [radians m^{-2}]	$\mathcal{U}[-110, 000, 110, 000]$	$-74, 582^{+419}_{-437}$	738.30/480	−2609.25	1297.00 ± 0.32
...	...	ψ_0 [deg]	$\mathcal{U}[0, 180]$	$75.36^{+2.25}_{-2.10}$	...	...	...
...	m11[b]	$p_{0,1}$ [%]	$\mathcal{U}[0, 100]$	$9.99^{+3.93}_{-2.07}$	...	...	...
...	...	$p_{0,2}$ [%]	$\mathcal{U}[0, 100]$	$6.63^{+3.85}_{-2.05}$	...	...	...
...	...	ϕ_1 [radians m^{-2}]	$\mathcal{U}[-110, 000, 110, 000]$	$-69, 767^{+1867}_{-2105}$	**338.00/477**	**−2965.25**	**1475.17 ± 0.40**
...	...	ϕ_2 [radians m^{-2}]	$\mathcal{U}[-110, 000, 110, 000]$	$-62, 047^{+3095}_{-2744}$	...	...	...
...	...	$\psi_{0,1}$ [deg]	$\mathcal{U}[0, 180]$	$34.27^{+9.84}_{-8.99}$	...	...	...
...	...	$\psi_{0,2}$ [deg]	$\mathcal{U}[0, 180]$	$72.58^{+11.86}_{-15.36}$	...	...	...
...			31–33 GHz data excluded from q–u fitting				
...	m1	p_0 [%]	$\mathcal{U}[0, 100]$	$4.88^{+0.06}_{-0.06}$	...	...	...
...	...	ϕ [radians m^{-2}]	$\mathcal{U}[-110, 000, 110, 000]$	$-74, 436^{+417}_{-431}$	612.89/354	−1836.14	909.95 ± 0.32
...	...	ψ_0 [deg]	$\mathcal{U}[0, 180]$	$74.05^{+2.26}_{-2.17}$	...	...	...
...	m11[b]	$p_{0,1}$ [%]	$\mathcal{U}[0, 100]$	$7.16^{+4.06}_{-1.68}$	...	...	...
...	...	$p_{0,2}$ [%]	$\mathcal{U}[0, 100]$	$5.43^{+3.97}_{-1.55}$	...	...	...
...	...	ϕ_1 [radians m^{-2}]	$\mathcal{U}[-110, 000, 110, 000]$	$-73, 689^{+2770}_{-2543}$	**214.02/351**	**−2192.23**	**1088.33 ± 0.39**

Table 4
(Continued)

Date	Model	Parameter	Prior	Posterior (68% CI)	χ^2/DOF	BIC	ln Evidence
...	...	ϕ_2 [radians m^{-2}]	$\mathcal{U}[-110, 000, 110, 000]$	$-81, 978^{+2567}_{-3717}$	...	...	...
...	...	$\psi_{0,1}$ [deg]	$\mathcal{U}[0, 180]$	$94.24^{+13.72}_{-14.02}$	...	...	...
...	...	$\psi_{0,2}$ [deg]	$\mathcal{U}[0, 180]$	$70.31^{+17.13}_{-15.49}$	...	...	...
2025 Apr 7	m1[b]	p_0 [%]	$\mathcal{U}[0, 100]$	$3.63^{+0.11}_{-0.11}$	...	...	...
...	...	ϕ [radians m^{-2}]	$\mathcal{U}[-110, 000, 110, 000]$	$-63, 790^{+3303}_{-3409}$	**261.80/488**	**−2355.35**	**1173.36 ± 0.29**
...	...	ψ_0 [deg]	$\mathcal{U}[0, 180]$	$62.64^{+9.16}_{-9.51}$	...	...	...
...	m11	$p_{0,1}$ [%]	$\mathcal{U}[0, 100]$	$4.07^{+3.09}_{-0.06}$	...	...	...
...	...	$p_{0,2}$ [%]	$\mathcal{U}[0, 100]$	$0.95^{+2.83}_{-0.72}$	...	...	...
...	...	ϕ_1 [radians m^{-2}]	$\mathcal{U}[-110, 000, 110, 000]$	$-65, 797^{+5909}_{-9832}$	400.41/485	−2343.36	1171.13 ± 0.32
...	...	ϕ_2 [radians m^{-2}]	$\mathcal{U}[-110, 000, 110, 000]$	$-70, 581^{+40,169}_{-27,866}$	...	...	...
...	...	$\psi_{0,1}$ [deg]	$\mathcal{U}[0, 180]$	$68.68^{+25.47}_{-17.90}$	...	...	...
...	...	$\psi_{0,2}$ [deg]	$\mathcal{U}[0, 180]$	$62.92^{+65.59}_{-39.66}$	...	...	...
2025 Apr 9	m1[b]	p_0 [%]	$\mathcal{U}[0, 100]$	$1.54^{+0.04}_{-0.04}$	...	...	...
...	...	ϕ [radians m^{-2}]	$\mathcal{U}[-110, 000, 110, 000]$	$-63, 873^{+1039}_{-1205}$	**261.78/474**	**−3306.87**	1646.38 ± 0.32
...	...	ψ_0 [deg]	$\mathcal{U}[0, 180]$	$63.47^{+6.13}_{-5.23}$	...	...	...
...	m11	$p_{0,1}$ [%]	$\mathcal{U}[0, 100]$	$1.49^{+0.06}_{-0.16}$	...	...	...
...	...	$p_{0,2}$ [%]	$\mathcal{U}[0, 100]$	$0.24^{+0.15}_{-0.07}$	...	...	...
...	...	ϕ_1 [radians m^{-2}]	$\mathcal{U}[-110, 000, 110, 000]$	$-68, 468^{+2723}_{-4235}$	317.07/471	−3308.82	**1648.87 ± 0.38**
...	...	ϕ_2 [radians m^{-2}]	$\mathcal{U}[-110, 000, 110, 000]$	$5034^{+18,400}_{-20,272}$	...	...	...
...	...	$\psi_{0,1}$ [deg]	$\mathcal{U}[0, 180]$	$85.91^{+21.11}_{-13.03}$	...	...	...
...	...	$\psi_{0,2}$ [deg]	$\mathcal{U}[0, 180]$	$97.41^{+56.43}_{-66.63}$	...	...	...

Notes. Bold numbers in the three rightmost columns indicate the model (m1 or m11) with the better goodness-of-fit value.
[a] Two constraints are used for the m11 fits: (1) $p_{0,1} + p_{0,2} \leqslant 100\%$ and (2) $\Delta p_0 = p_{0,1} - p_{0,2} \in [0\%, 100\%]$ (i.e., so $p_{0,1} \geqslant p_{0,2}$).
[b] Chosen best-fit model for each observation.

ORCID iDs

Joseph M. Michail https://orcid.org/0000-0003-3503-3446
Sebastiano D. von Fellenberg https://orcid.org/0000-0002-9156-2249
Mayura Balakrishnan https://orcid.org/0000-0001-9641-6550
Geoffrey C. Bower https://orcid.org/0000-0003-4056-9982
Nicole M. Ford https://orcid.org/0000-0001-8921-3624
Zach Sumners https://orcid.org/0009-0004-8539-3516
Giovanni G. Fazio https://orcid.org/0000-0002-0670-0708
Daryl Haggard https://orcid.org/0000-0001-6803-2138
Joseph L. Hora https://orcid.org/0000-0002-5599-4650
Garrett K. Keating https://orcid.org/0000-0002-3490-146X
J. D. Livingston https://orcid.org/0000-0002-4090-8000
Sera Markoff https://orcid.org/0000-0001-9564-0876
Bart Ripperda https://orcid.org/0000-0002-7301-3908
Sophia Sánchez-Maes https://orcid.org/0000-0002-0947-569X
S. P. Willner https://orcid.org/0000-0002-9895-5758
Jun-Hui Zhao https://orcid.org/0000-0002-1317-3328

References

Abbate, F., Noutsos, A., Desvignes, G., et al. 2023, MNRAS, 524, 2966
Astropy Collaboration, Price-Whelan, A. M., Lim, P. L., et al. 2022, ApJ, 935, 167
Astropy Collaboration, Price-Whelan, A. M., Sipőcz, B. M., et al. 2018, AJ, 156, 123
Astropy Collaboration, Robitaille, T. P., Tollerud, E. J., et al. 2013, A&A, 558, A33
Blandford, R. D., & Königl, A. 1979, ApJ, 232, 34
Bower, G. C., Backer, D. C., Zhao, J.-H., Goss, M., & Falcke, H. 1999, ApJ, 521, 582
Bower, G. C., Broderick, A., Dexter, J., et al. 2018, ApJ, 868, 101
Bower, G. C., Wright, M. C. H., Falcke, H., & Backer, D. C. 2003, ApJ, 588, 331
Brentjens, M. A., & de Bruyn, A. G. 2005, A&A, 441, 1217
Brocksopp, C., Corbel, S., Tzioumis, A., et al. 2013, MNRAS, 432, 931
CASA, T., Bean, B., Bhatnagar, S., et al. 2022, PASP, 134, 114501
Condon, J. J., & Ransom, S. M. 2016, Essential Radio Astronomy (Princeton Univ. Press)
Degenaar, N., Reynolds, M. T., Wijnands, R., et al. 2016a, ATel, 1, 9109
Degenaar, N., Reynolds, M. T., Wijnands, R., et al. 2016b, ATel, 9196, 1
Desvignes, G., Eatough, R. P., Pen, U. L., et al. 2018, ApJL, 852, L12
Dickey, J. M., Landecker, T. L., Thomson, A. J. M., et al. 2019, ApJ, 871, 106
Eatough, R. P., Falcke, H., Karuppusamy, R., et al. 2013, Natur, 501, 391
GRAVITY Collaboration, Abuter, R., Amorim, A., et al. 2019, A&A, 625, L10
Grollimund, N., Corbel, S., Bahramian, A., et al. 2025, ATel, 17045, 1
Hannikainen, D. C., Hunstead, R. W., Campbell-Wilson, D., et al. 2000, ApJ, 540, 521
Heinke, C. O., Nakajima, M., Kudo, Y., et al. 2025, ATel, 17010, 1
Hughes, A. K., Sivakoff, G. R., Macpherson, C. E., et al. 2023, MNRAS, 521, 185
Jaisawal, G. K., Steiner, J. F., Strohmayer, T. E., et al. 2025, ATel, 17040, 1
Kepley, A. A., Tsutsumi, T., Brogan, C. L., et al. 2020, PASP, 132, 024505
Koposov, S., Speagle, J., Barbary, K., et al. 2022, joshspeagle/dynesty: v1.2.1,
Kudo, Y., Negoro, H., Nakajima, M., et al. 2025, ATel, 16975, 1
Lacy, M., Baum, S. A., Chandler, C. J., et al. 2020, PASP, 132, 035001
Liu, H. B., Wright, M. C. H., Zhao, J.-H., et al. 2016, A&A, 593, A107
Longair, M. S. 2011, High Energy Astrophysics (Cambridge Univ. Press)
Mandel, S., Mori, K., Ciurlo, A., et al. 2025a, arXiv, arXiv:2509.14465
Mandel, S., Mori, K., Hailey, C., et al. 2025b, ATel , 17063, 1
Mandel, S., Mori, K., Hua, Z., et al. 2026, ATel, 17663, 290037, 1
Mandel, S., Levin, B., Mori, K., et al. 2025c, ATel , 17087, 1
Marra, L., Mikušincová, R., Vincentelli, F. M., et al. 2026, ApJ, 1001, 178
Marrone, D. P., Moran, J. M., Zhao, J.-H., & Rao, R. 2006, ApJ, 640, 308
Marrone, D. P., Moran, J. M., Zhao, J.-H., & Rao, R. 2007, ApJL, 654, L57

Michail, J. M., von Fellenberg, S., Haggard, D., et al. 2025, ATel , 17174, 1
Michail, J. M., von Fellenberg, S. D., Keating, G. K., et al. 2026, ApJ, 997, 282
Miller-Jones, J. C. A., Tetarenko, A. J., Sivakoff, G. R., et al. 2019, Natur, 569, 374
Mori, K., Hailey, C. J., Mandel, S., et al. 2019, ApJ, 885, 142
Nakajima, M., Negoro, H., Kudo, Y., et al. 2025, ATel , 16983, 1
O'Sullivan, S. P., Brown, S., Robishaw, T., et al. 2012, MNRAS, 421, 3300
Purcell, C. R., Van Eck, C. L., West, J., Sun, X. H., & Gaensler, B. M. 2020, RM-Tools: Rotation measure (RM) synthesis and Stokes QU-fitting, Astrophysics Source Code Library, ascl:2005.003
Rodriguez Cavero, N. 2024, arXiv, arXiv:2402.10371
Roy, S., Pramesh Rao, A., & Subrahmanyan, R. 2008, A&A, 478, 435
Roychowdhury, T., von Fellenberg, S. D., Michail, J. M., et al. 2025, PASP, 137, 114102
Rybicki, G. B., & Lightman, A. P. 1986, Radiative Processes in Astrophysics (Wiley-VCH)
Sault, R. J., Hamaker, J. P., & Bregman, J. D. 1996, A&AS, 117, 149
Sicheneder, E., & Dexter, J. 2017, MNRAS, 467, 3642
von Fellenberg, S. D., Roychowdhury, T., Michail, J. M., et al. 2025, ApJL, 979, L20
Wang, Y., Coti Zelati, F., Rea, N., et al. 2025, ATel, 17068, 1
Watanabe, S., Aoyama, A., Takeda, T., et al. 2025, ATel, 17009, 1
Yusef-Zadeh, F., Diesing, R., Wardle, M., et al. 2015, ApJL, 811, L35
Zdziarski, A. A., Tetarenko, A. J., & Sikora, M. 2022, ApJ, 925, 189